Article

Developed Brinkman Model into a Porous Collector for Solar Energy Applications with a Single-Phase Flow

Mojtaba Rezapour [1], Sayyed Aboozar Fanaee [1] and Maryam Ghodrat [2,*]

1 Department of Mechanical Engineering, University of Birjand, Birjand 97175615, Iran
2 School of Engineering and Information Technology, University of New South Wales, Canberra, ACT 2612, Australia
* Correspondence: m.ghodrat@unsw.edu.au

Abstract: In this paper, the effects of the fluid-thermal parameters of a porous medium with different values of porosity and permeability on the fluid flow, heat, and concentration parameters were investigated for solar energy applications. The characteristics of the boundary layer, velocity profiles, pressure drop, and thermal and high heat concentration distribution have been analyzed. A developed Brinkman equation for fluid flow and a power law model for thermal conductivity (considering the porosity and permeability factors) were calculated with constant solar heat flux. The numerical model was developed based on the finite element method by the LU algorithm using the MUMPS solver. The Brinkman equations were solved under steady and unsteady states for velocity, pressure, thermal, and concentration distribution effects, respectively. In a porous medium, the normalized temperature of the presented model had an acceptable agreement with the experimental data, with a maximum error of 3%. At constant permeability, by decreasing the porosity, the velocity profile was extended. This was mainly due to the presence of pores in the collector. With an accelerated flow, the maximum velocity of 2.5 m/s occurred at a porosity of 0.2. It was also found that in the porous collector, the Nusselt number increased where the maximum difference between the porous and the nonporous collectors occurred at the beginning of the collector, with a value of 32%, and the minimum difference was 27%. The results also indicate that in the porous collector, solar energy absorbance was higher and the heat transfer was improved. However, an increase in the pressure drop was noted in the porous collectors.

Keywords: solar collector; porous medium; developed brinkman equation; mass-fluid analysis

1. Introduction

Nowadays, porous metal environments have important roles in a wide range of industrial equipment that can be used in a variety of applications [1]. The composition of these mediums with nanofluid flows can be considered to improve the efficiency of thermal systems. Bayomy and Saghir [2] conducted an experimental study of alumina nanofluid in a porous micro-channel for a low volumetric percentage of nanofluid to analyze the thermal conductivity of a metal foam with a four-core processor. The results of this work showed that the Nusselt number of flows increased using the nanofluids. Boomsma and Poulikakos [3] developed a 3D model of the thermal conductivity of a porous foam saturated on the basis of its porous geometry. The geometric shape of the filling of a given space with same-sized pores that produced a minimum porosity surface was estimated in the work, and basic definitions for effective thermal conductivity for various foams were reported. In [4], different forms of a flow equation into a porous medium as an alternative to the Navier–Stokes equation for single-phase conditions were discussed. Dukhan and Chen [5] examined a simple model of airflow and heat transfer into aluminum metal foams and described how the temperature was distributed. Their model consisted of a fixed flux exerted on the wall of a channel. Dukhan and Ratowski [6] (2010)

developed an analytical solution for a solid-state energy equation for a porous medium that was placed in a two-dimensional fashion under constant heat flux. The most important achievement of the study was its examination of the capability of the equipment to be cooled down by fluid by changing its thermal conductivity coefficient. Furman et al. [7] examined the methods for producing porous aluminum foams and analyzed parameters such as the penetrability of foam with a porosity of more than 60%. Guo and Yu [8] analyzed pipes filled with metal foam under different dynamic loading levels. They found that the deformation of porous foam with a dynamic loading is completely different. Hamdan [9] examined the flow of single-phase fluid into a porous medium and showed that when the flow was fully developed, the conditions of entering a porous channel with different flow models were compatible with Navier–Stokes equation conditions. Lu and Tassou [10] analyzed the properties of forced heat transfer in different porosity foamed tubes, and they studied the Darcy model for moving flows into this medium. Furthermore, in this solution, two different equations for solid and fluid heat transfers into the porous medium were used. Their results showed that pore size and porosity of metal foams played important roles in the overall performance of heat exchange from the tubes. Mancin et al. [11] measured the heat transfer and pressure loss of copper foams in a laboratory setup and found that the heat transfers and fluid flows in metal foams were increased compared to those of the non-porous medium. In addition, in another application of a porous medium, the analysis of a hydrogen–air mixture passing through aluminum foam was investigated by Rezapour and Fanaee [12], aiming to use porous foams in hydrogen fuel cell electrodes. In this work, the influences of key parameters on the flow and heat transfer in the porous medium were discussed. Nakayama and Shenoy [13] studied an analytical fluid in a saturated porous medium and examined the effects of the boundary layer in this environment. In their paper, the equations for free heat transfer in a porous medium and the effect of a Peclet number based on the slip wall conditions were analyzed. Özgümüş et al. [14] investigated experimental methods for determining the axial and transverse thermal dispersions inside coils and reported on their experimental method for determining the heat dispersion coefficient. Pankaj and Malipatil [15] studied the properties of heat transfer in four different aluminum foams. The experiments were carried out to measure the pressure drop in the metal foam and the heat transfer coefficient with a mass flow rate from 0.002 to 0.11 (kg/s). Fanaee and Rezapour [16] defined a thermal transition region within the porous medium with a continued Stokes equation. This work led to the development of a developed Brinkman method for fluid in a porous medium. Zhong et al. [17] found that the compression effect could exacerbate the pressure drop. It has also been proven that there is a wide range of transient diameters in which the wall effect is physically ineffective in terms of pressure and temperature. Yang and Nakayama [18] analyzed the chemical composition and its dispersion on the effective thermal conductivity of porous media, and they used the theory of average volume distribution in an analytical manner. The physics and fundamental definitions of parameters in porous media, as well as various forms of equations in a porous medium, were expressed in [19]. Huijin et al. [20] examined the boundary layer in a porous medium by external flow equations. They also examined the flow and heat transfer of the Prandtl and Peclet numbers. Dushin et al. [21] pursued mathematical modeling in a porous medium for a two-dimensional and three-dimensional solutions. Nakayama and Shenoy [22] examined the forced heat transfer of non-Darcy flow in a two-dimensional channel with thermal flux. One of the most important results of this work was the introduction of a relation for a Nusselt number based on Reynolds number variations. Cummins [23] analyzed an unstoppable flow in a porous medium with different pore sizes using a model that was based on the Darcy equation. Fanaee and Rezapour [24] modeled a CPVT system with the shadow effects of a solar porous collector on the concentrator. Their work showed that heat flux can be considerably powered by using parabolic concentrators. Zehforoosh et al. [25] investigated forced convective heat transfer with laminar and steady fluid flows. Dukhan et al. [26] analyzed heat transfer in a tube filled with metal foam. They found that the thermal

entry region in the metal foam was significant and much longer. Other researchers such as Cummins et al. [23] have explored unsteady flow in porous media with different pore sizes based on their Darcy equation model. This study showed that heterogeneous porous material is neither fully saturated nor constantly saturated behind the visible wetted front. Zafariyan et al. [27] studied the effects of Soret and Dufour numbers on a mixed flow over a vertical plate embedded in a porous medium. In another work, Zafariyan and Fanaee [28] analyzed the effects of thermal radiation on steady mixed convection flows with a plate embedded into a porous medium. These two works showed a good applicability of time-dependent mass and stabilized energy and momentum solutions into a porous medium. Various numeric and experimental studies have been performed on solar systems [29,30]. One of the effective parameters of the efficiency of CPVT systems is a type of concentrator or photovoltaic cell [31–33]. Kuzmenkov et al. [34] numerically studied direct absorption solar collectors (DASC) for different applications using computational fluid dynamics. Huang et. al. [35] evaluated concentrating fluid-based spectral-splitting hybrid PV-thermal collectors that can provide high electrical and thermal efficiencies. Their model of the collector with an optimal filter had a significantly higher total effective efficiency than an equivalent conventional solar-thermal collector. Alves et al. [36] studied the performance of a CPV/T and the thermal effects on its energy efficiency using an electromagnetic-thermal finite element model in Swedish and Portuguese climate zones.

The presented literature review indicates that despite a number of studies being performed in the domain of fluid flow and heat transfer in porous media, the basic understanding of mass transfer requires further investigation, particularly with respect to parameters such as permeability and porosity on concentrated distributions in porous media. In previous works, experimental and numerical data on the impacts of the effect of mass transfer in porous media were investigated; however, the fundamental reasons and main reactions between fluid-thermal parameters and occurrence are unclear.

This work aims to close this research gap by providing a quantitative and systematic analysis of porous media applications. The main objectives of this study are to provide a thorough insight into the fluid-thermal analysis of a porous collector. A computational fluid dynamics method is developed to quantitatively investigate the effects of velocity profiles, pressure drop, boundary layer, and solar heat flux on the time-dependent flow concentration.

2. Model Description

The geometry of the present model consists of a porous aluminum collector with a square cross-section. In Figure 1, a schematic diagram of the structure is shown. The length and height of the collector are equal to L and H, respectively. The boundary conditions for the fluid analysis are included as the inlet velocity u_{in}, the output pressure Pout, and the no-slip boundary condition for the wall. For thermal analysis, the boundary conditions include the inlet fluid temperature T_{in} and zero gradients of temperature at the outlet of the collector. Furthermore, a solar heat flux with an average value of Q″, which is prepared by a parabolic concentrator, is entered on the wall of a porous collector. For concentration analysis, the boundary conditions include C_{in} for the inlet concentration and outflow boundary condition at the outlet, with an initial zero concentration.

Figure 2 shows a sample of a porous collector where the collector is filled with aluminum foam. The effective thermal conductivity of the porous collector is considered as k_{eff}, which is determined from the porosity percentage; ε, which is the thermal conductivity of the aluminum foam, k_p; and the thermal conductivity of the fluid, k.
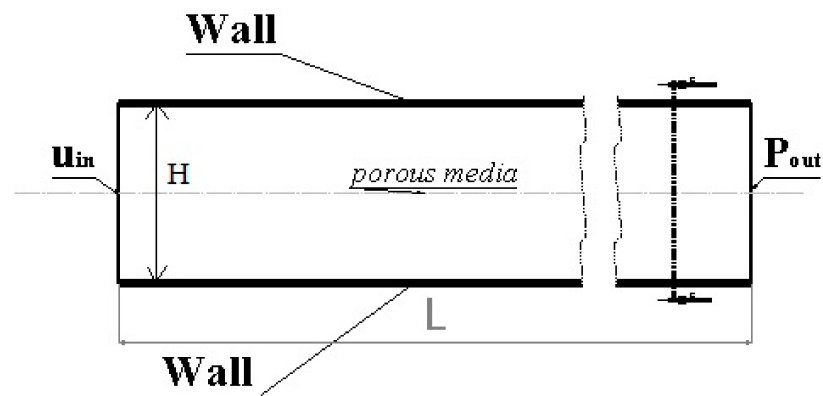
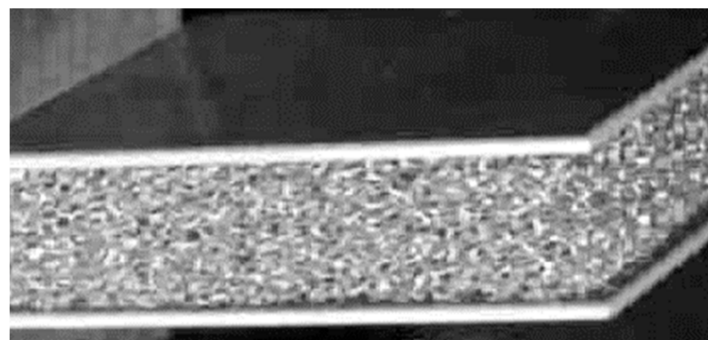**Figure 1.** The schematic diagram of the modeling structure.

Figure 2. A sample of the metal porous collectors in the presented model.

3. Governing Equations

To analyze the porous collector, the continuity equation and the developed Brinkman analysis of fluid were considered [4]. The unsteady forms of these equations were used for coupling with momentum, concentration, and energy equations, written as follows:

$$\frac{\partial}{\partial t}(\rho\varepsilon) + \nabla\cdot(\rho u) = 0 \tag{1}$$

$$\frac{\rho}{\varepsilon}\left(\frac{\partial u}{\partial t} + (u\cdot\nabla)\frac{u}{\varepsilon}\right) = -\nabla\left[p + \frac{\mu}{\varepsilon}\left(\nabla u + (\nabla u)^T\right) - \frac{2}{3}\frac{\mu}{\varepsilon}(\nabla\cdot u)\right] - \left[(K^{-1}\mu)u\right] \tag{2}$$

where ε, Q, C_P, μ, and u are the porosity, density, specific heat capacity, dynamic viscosity, and average velocity of the flow, respectively. The permeability of the porous collector, K, was considered a constant that was formulated from an experimental estimation, as follows [4]:

$$K = \frac{D_p{}^2\varepsilon^3}{a(1-\varepsilon)^2} \tag{3}$$

where, considering Carmen's theory, a is equal to 180 and D_p is the average diameter of the porous media holes.

The energy equation was considered according to the following equation [4]:

$$(\rho c_p)_{eff}\frac{\partial T}{\partial t} + (\rho c_p)_{eff}(u\frac{\partial T}{\partial x} + v\frac{\partial T}{\partial y}) = \nabla\cdot(k_{eff}\nabla T) + Q \tag{4}$$

In the above equation, Q is the volume heat source term in the solar collector that was considered equal to zero. Furthermore, u represents the average velocity of flow into the porous collector that was obtained from Equation (5):

$$u = \varepsilon v \tag{5}$$

In Equation (4), the value of k_{eff} is calculated with the help of the thermal conductivity of the fluid, k, and the thermal conductivity of the aluminum foam, k_p, in accordance with Equation (6) (derived from [4]):

$$k_{eff} = k_p{}^{\varepsilon} \cdot k^{(1-\varepsilon)} \qquad (6)$$

The convection heat transfer coefficient was calculated by considering the temperature differences between the centerline, T_f, and the wall, T_W, of the collector at each specified section and entering the solar heat flux from the top surface of the collector, Q'', as presented in Equation (7) [24,37]:

$$h(x) = \frac{Q''}{(T_w - T_f)} \qquad (7)$$

The Nusselt number was dependent on the convection heat transfer coefficient, as shown in Equation (8) [24,37]:

$$Nu_D(x) = \frac{h(x) \cdot H}{k} \qquad (8)$$

The normalized width, Y, and temperature, θ, were obtained in accordance with Equations (9) and (10) from [5], respectively:

$$Y = \frac{y}{H} \qquad (9)$$

$$\theta = \frac{T - T_i}{(Q'' H / k_{eff})} \qquad (10)$$

In these equations, H is the channel height, y is the perpendicular coordinate of the channel, and T_i is the inlet flow temperature.

The governing equation of concentration for the porous collector was calculated as follows [4]:

$$(\varepsilon + \rho_b k_{p,i})\frac{\partial c}{\partial t} + (c + \rho_b C_p)\frac{\partial \varepsilon}{\partial t} + \nabla \cdot ((-D_D + D_\varepsilon)\nabla c) + u \cdot \nabla c = R_i + S_i \qquad (11)$$

$$D_\varepsilon = \frac{\varepsilon}{\tau_F} D_F \qquad (12)$$

In these equations, D_D is the dispersion coefficient, D_F is the fluid diffusivity coefficient, D_e is the total diffusivity coefficient, C is the concentration, and τ_F is the effective mass diffusivity coefficient. The values of τ_F were calculated from the Brugman model, as presented in Equation (13) [4]:

$$\tau_F = \varepsilon^{-1/2} \qquad (13)$$

For thermal and fluid analysis, unsteady solutions of these equations and steady-state responses were used, while the time-dependent response of the concentration presented the trend of the fluid flow variation.

4. Results and Discussion

In the current study, the effects of porous media with different values of porosity and permeability on fluid flow, heat, and concentration parameters were calculated into a solar collector. A developed Brinkman equation was considered for fluid flow analysis, and the power law equation and Brugman model were taken into account for the effective thermal conductivity and effective mass coefficient calculations, respectively. The collector walls were exposed to the constant solar heat flux powered by a parabolic concentrator. The length of the collector was 1200 mm and the height was equal to 50.8 mm. The numerical model was based on the finite element method by lower–upper (LU) factorization using the multi-frontal massively parallel sparse (MUMPS) solver. This solver is a direct program that works based on numerical coding, which is a subset of the finite element method.

4.1. Validation

For validation of this model, as seen in Figure 3, the results of the normalized temperature of the airflow into an aluminum foam collector with dimensions of $6 \times 10 \times 5$ cm and a porosity of 79.6% in similar conditions to [5] were calculated. According to this figure, the results of the present model were in good agreement with the experimental data of [5], where the maximum error was equal to 3%. Furthermore, the present data were closer to the experimental data than the numerical model of [5], where the maximum deviation between the experimental data and the numerical model was equal to 14% at $Y = 0.82$. Considering this, the improvement of this model compared to other models of the numerical solution of the fluid flow inside the porous medium are shown. In addition to the present model, it can be used in most of the fluid flows in a porous medium.
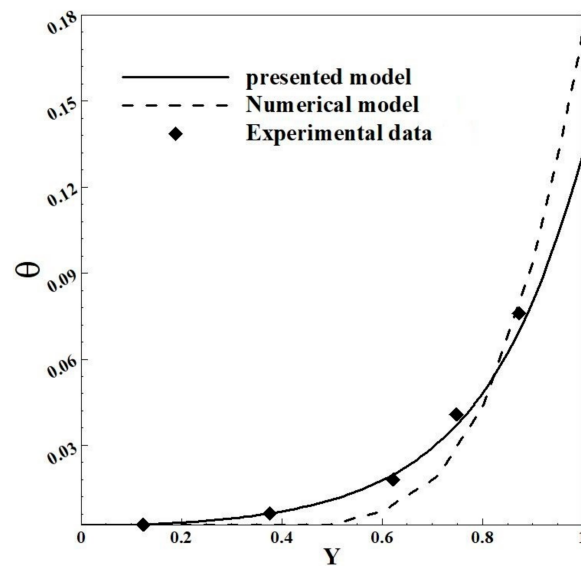
Figure 3. The comparison between the normalized temperature achieved from the present model and the numerical and experimental data [5] for air flow into an ERG aluminum porous foam at $\varepsilon = 79.6\%$.

4.2. Grid Sensitivity Analysis

To verify the independence of the grid from the numerical solution, the responses of the convective heat transfer for three different triangular grids with 5502, 27,491 and, 63,432 nodes are compared in Figure 4. As shown, the response was significantly affected by the number of grids in that once the number of nodes had changed from coarse, with 5502 nodes, to the average grid, with 27,491 nodes, the values of the convection heat transfer coefficients were completely altered, showing dependence on the used grid number at this domain. However, for fine mesh with 63,432 nodes, the response was not considerably changed relative to the average grid. Therefore, the results were calculated for the selected average grid.

4.3. Results and Discussion

To investigate the heat transfer problem in the porous collector for porous and non-porous conditions, the variation in the Nusselt number in terms of the length to height ratio of the collector is shown in Figure 5. The variation in the Nusselt number was calculated with help of Equations (7) and (8). The collector was placed under a constant solar heat flux of 20 W/cm^2 that was prepared by a parabolic concentrator. As seen in this figure, by increasing the length to height ratio of the channel, the Nusselt number decreased as result of the decreasing difference between the wall and the fluid temperature in the collector. The Nusselt number value in the porous collector was higher than that of the non-porous collector, with a maximum difference of 32% at the beginning of the collector.

This increase improved the heat transfer to the fluid for the porous collector conditions that corresponded to the increase in the pressure drop. Furthermore, comparing the variation in the convection heat transfer and the Nusselt number, as seen in Table 1, the convective heat transfer coefficient for the porous collectors was also larger than that of the non-porous collectors. This was mainly due to the effects of porosity and high-temperature gradient from the heat flux to the working fluid in the porous collector.
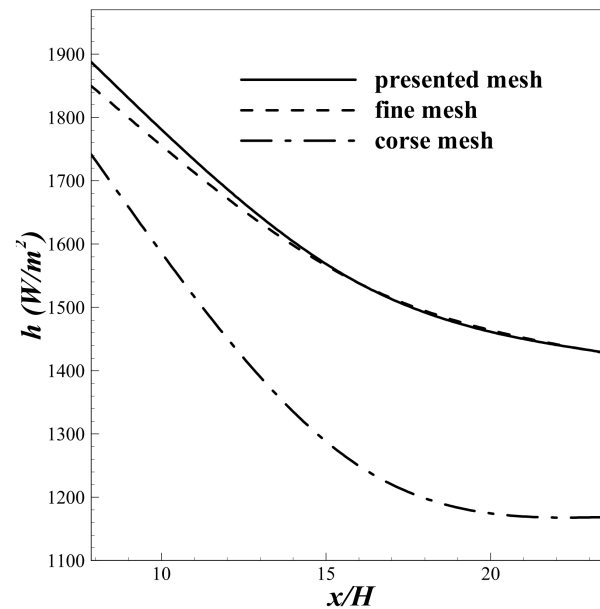
Figure 4. The study of grid independency for the presented solution considering three different unstructured grids with 63,432 (fine), 27,491 (average), and 5502 (coarse) nodes.
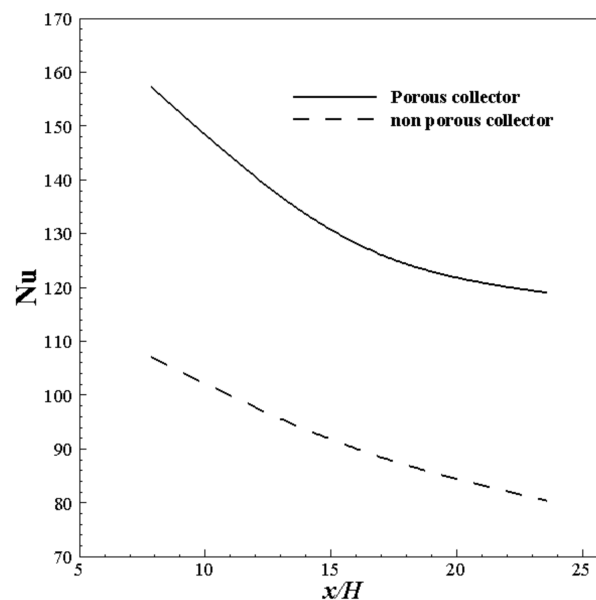

Figure 5. The variation in the Nusselt number versus the length to height ratio into porous and non-porous collectors at u_{in} = 0.5 m/s, T_{in} = 298, ε = 0.8, and K = 6 $\times$ 10^{-10} m^2.

Table 1. The comparison between the convection heat transfer coefficient and the Nusselt number for porous and non-porous collectors, with L = 500 mm.

| Collector	$h\left(\frac{W}{m^2 \cdot K}\right)$	Nu
Porous collector	1787.31	148.94
Nonporous collector	1229.40	102.45

Figure 6 shows the normalized velocity profile for a constant permeability of 5×10^{-6} m^2 and a different porosity into a solar collector with a length of 500 mm and inlet velocity of 2 m/s. According to the results presented in this figure, the velocity profile was stretched with the decrease in the porosity coefficient of the collector such that the flow accelerated, with a maximum velocity of 2.5 m/s and a porosity coefficient of 0.2.
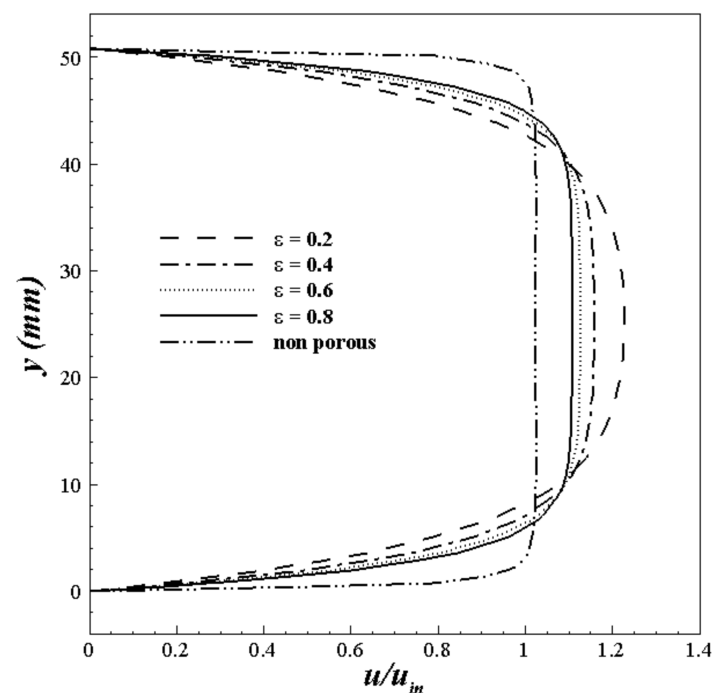
Figure 6. The variation in velocity profile at a permeability of 5×10^{-6} m^2 and different porosity coefficients for non-porous and porous collectors, where u_{in} = 2 m/s and L = 500 mm.

Furthermore, the shear stress on the wall increased with the decreasing porosity. This was mainly due to the resulting decrease in the empty space, which led to more contact between the fluid and the walls and increased the shear stress. However, for the non-porous collectors, the profile was wider, with a maximum velocity of 1.3 m/s.

Figure 7 shows the curves of the velocity profile and the maximum of the boundary layer versus the porosity coefficients and a permeability of 6×10^{-6} m^2. According to the findings presented in this figure, by increasing the porosity coefficient, the velocity into the boundary layer decreased, and as a result, the boundary layer also decreased. In addition, with the increasing porosity, the flow conditions approached the non-porous collector, and so by reaching a porosity coefficient of 1, the boundary layer and velocity profile showed a similar trend to the non-porous collector, while the value of the porosity ratio was close to 1.
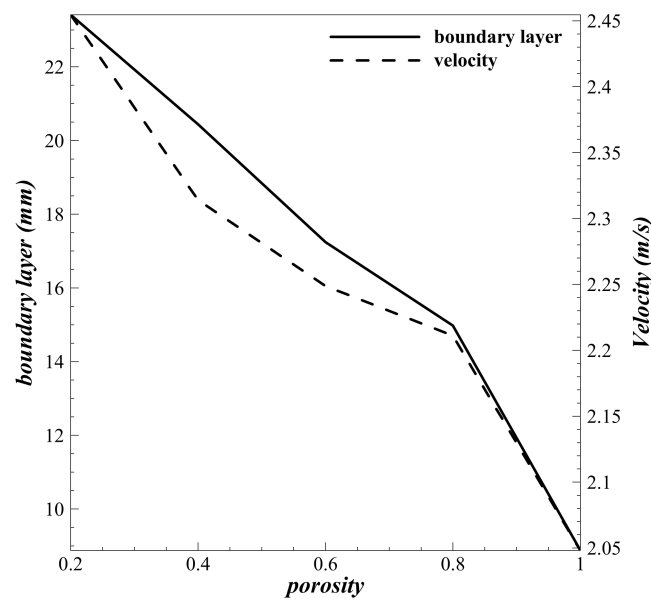
Figure 7. The variation in the velocity and maximum thickness of the boundary layer versus the porosity for a permeability of 5×10^{-6} m^2, with u_{in} = 2 m/s.

Figure 8 shows the variations in the pressure gradient across the collector with a permeability of 5×10^{-6} m^2 at the different values of the porosity coefficients. As shown, the pressure drop across the collector decreased with the increasing porosity coefficient such that the pressure drop for all porous conditions was greater than that of the non-porous collector because of the solid holdback effects into the porous medium. Furthermore, in a porous collector, the variation in average pressure is nearly linear, whereas this profile was not uniformly changed for the non-porous conditions. Increasing the pressure drop can lead to an increase in heat transfer from the wall to the porous collector channel.
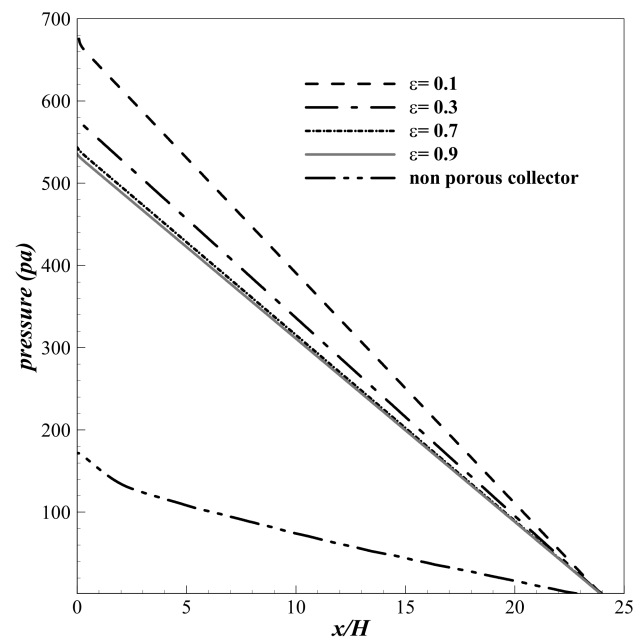
Figure 8. The variation in pressure across the collector versus the length to height ratio for the different porosity coefficients at a permeability of 5×10^{-6} m^2, with u_{in} = 2 m/s.

Figure 9 shows the velocity profiles for different values of permeability at the location of 500 mm in the length of the collector for the high and low porosity coefficients with

values of 0.8 and 0.2. As shown, the velocity profiles were stretched out by increasing the permeability. The extension was due to the increase in shear stress on the wall of the collector. Furthermore, increasing the amount of permeability increased the maximum velocity, but the velocity profile was stretched out by decreasing the porosity coefficient. This was mainly due to the fact that the shear stress was reduced by increasing the porosity because of the increasing empty spaces and contact surfaces between the flow and the solid.

(a) $K = 2 \times 10^{-6}$

(b) $K = 4 \times 10^{-6}$

(c) $K = 6 \times 10^{-6}$

(d) $K = 8 \times 10^{-6}$
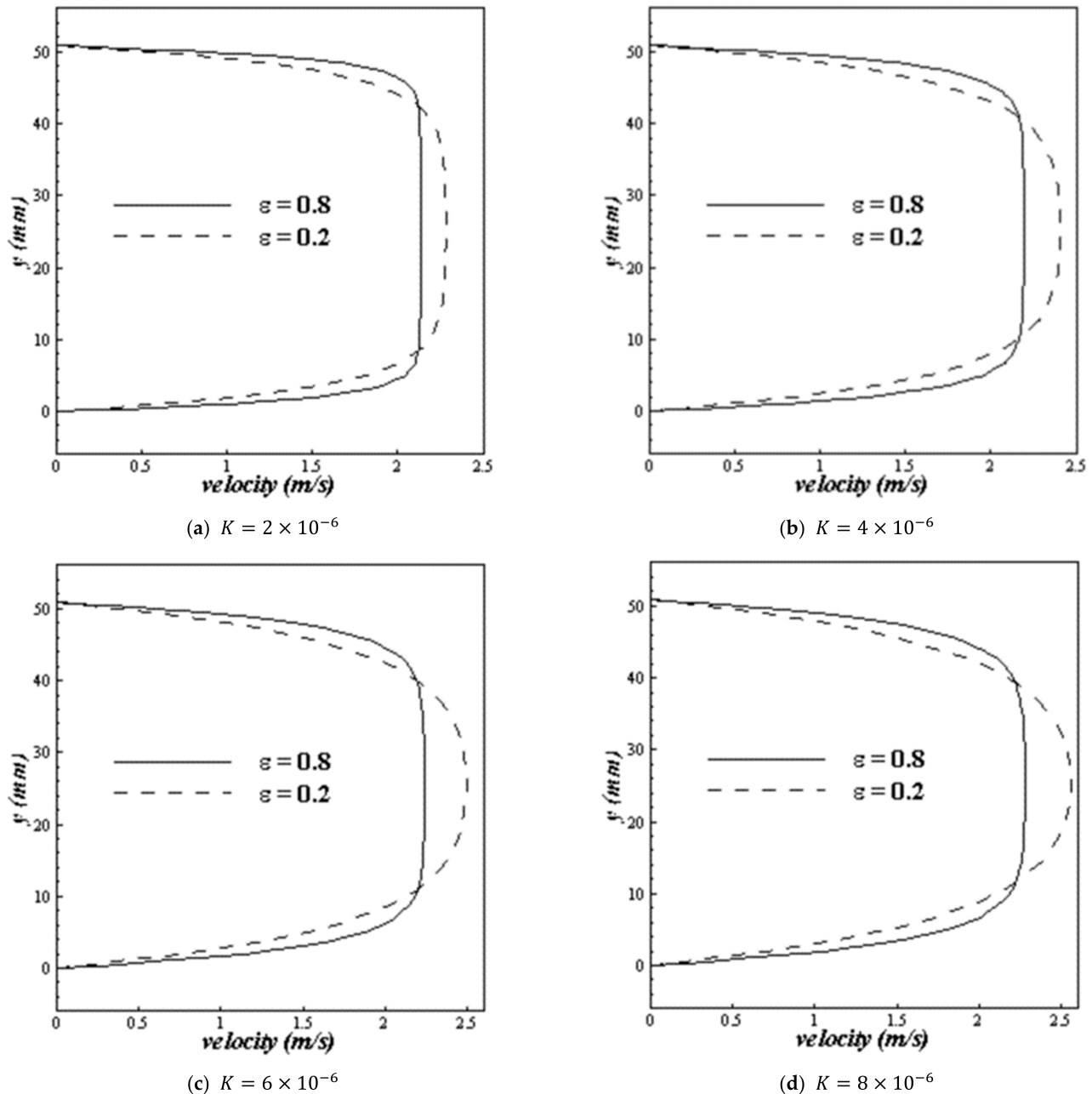
Figure 9. The variation in velocity profiles for the different values of permeability at the location of 500 mm in the length of the collector for the high, 0.8, and low, 0.2, porosity coefficients, with $u_{in} = 2$ m/s.

In Figure 10, the variation in pressure across the solar collector for different values of permeability at the location of 500 mm of the length of the collector is shown for the high and low porosity coefficients with values of 0.8 and 0.2. As shown, with increasing the permeability, the pressure was decreased, and the slope of the pressure curve significantly

changed with a maximum value of 34%. The graphs in Figures 8 and 10 show that the porosity and permeability of the porous collector changed the pressure linearly. The linear relation was due to the nearly constant shear stress at the different amounts of the porosity and permeability coefficients.
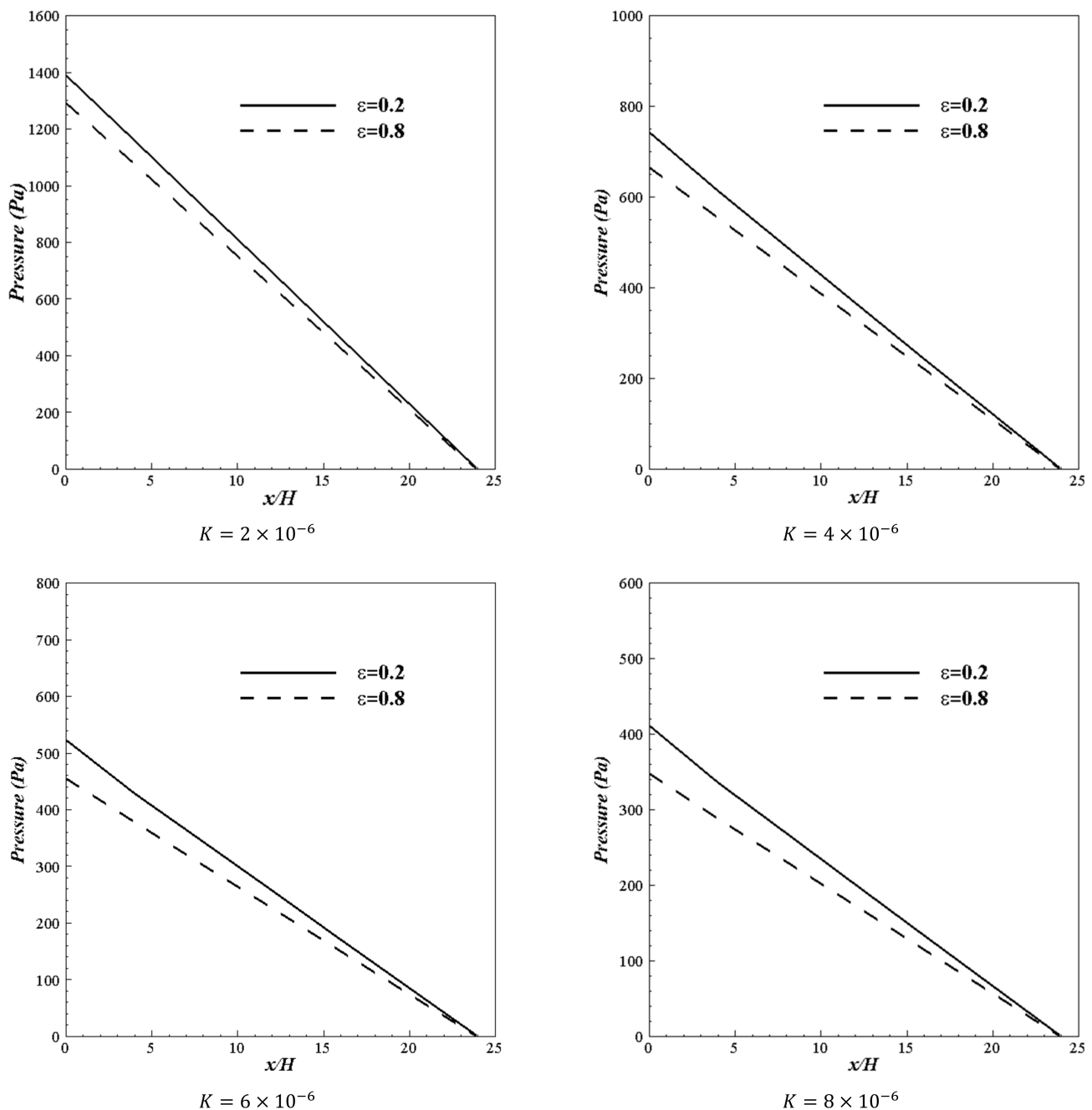
Figure 10. The variation in pressure across the collector versus the length to height ratio for the different values of permeability at the high, 0.8, and low, 0.2, porosity coefficients, with $u_{in} = 2$ m/s.

The time-dependent variations in concentration can present a complete approach to flow movement into the solar collector. The variations were calculated by considering the developed Brinkman model for the momentum and energy equations. Figure 11 shows the concentration contours in the porous collector for three different times and for a low porosity coefficient of 0.2. The distribution was affected by the temperature gradient made by the solar heat flux, considering the coupling of mass, momentum, and energy
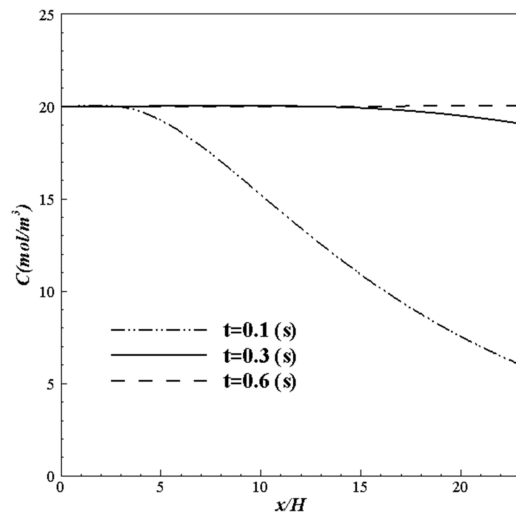
equations. This is the main reason for the stretched-out concentration profile at the three different times.
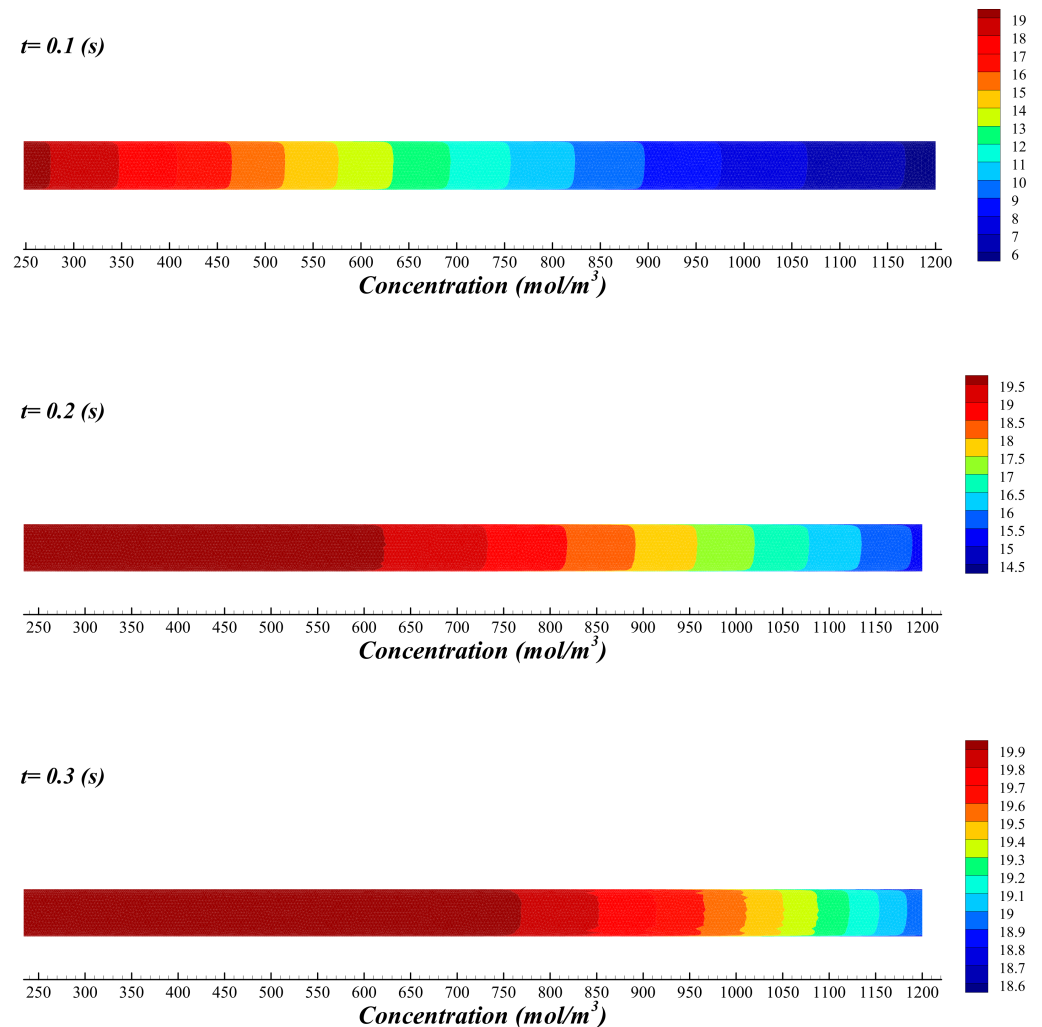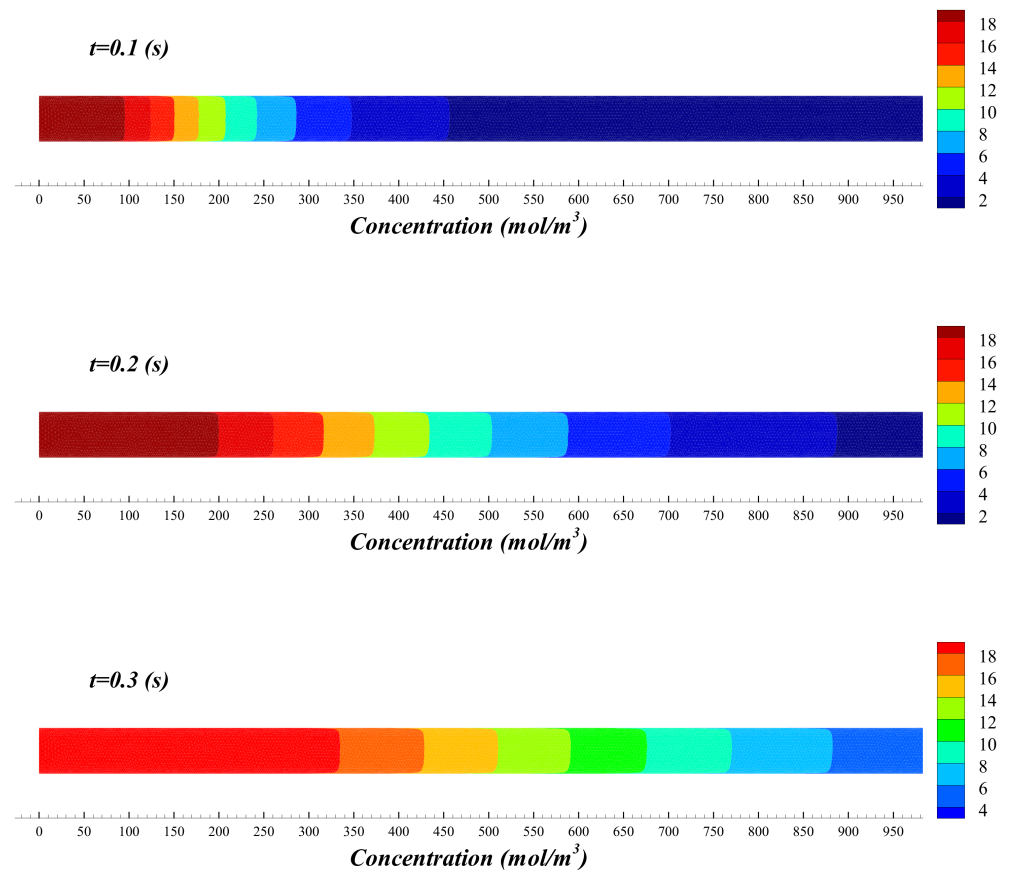

Figure 11. The contours of concentration in the porous collector at the three different time steps for a low porosity of 0.2.

Figure 12 shows the variation in the concentration versus the length to height ratio of the porous collector for the three different time steps, with a low porosity coefficient of 0.2. At x/H = 15, the amount of concentration changed to 11, 20, and 20 (mol/m^3) during 0.1, 0.3, and 0.6 (s), respectively. According to the results presented in this figure, with increasing time, the H_2O was diffused into the collector. Furthermore, at this low porosity, the flow would completely diffuse at approximately 0.6 s.

Figure 13 shows the contour of the H_2O concentration in the porous collector for three different times, with a high porosity of 0.8. As seen, the gradient of concentration was determined by the shear stress term near the wall. The concentration profile stretched out in the longitudinal direction. As the time increased, the concentration profile in the longitudinal direction stretched out at a faster pace than the high porosity condition, but the concentration magnitude remained constant.
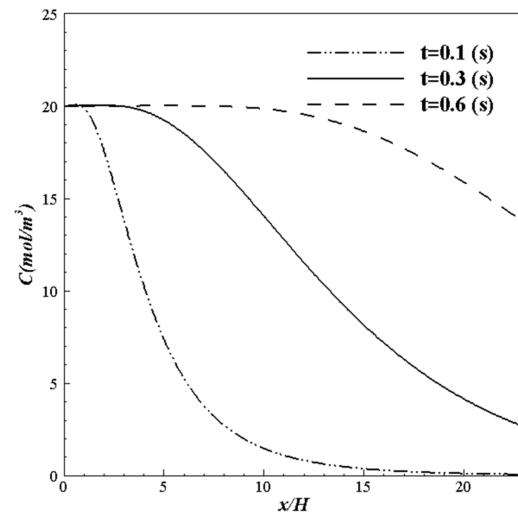
Figure 12. The variation in concentration in the porous collector for the three different times, with a low porosity coefficient of 0.2.

Figure 13. The contours of concentration in the porous collector at the three different times for a high porosity of 0.8.

The variation in the concentration versus the length to height ratio of the porous collector for three different times, with a high porosity of 0.8, is shown in Figure 14. According to the results presented in this figure, by time, H_2O was diffused into the collector; however, because of the high porosity of the medium, the mass flow would not completely diffuse at 0.6 s. The contours and distribution of concentration are plotted at similar times for both the low and high porosities of the collector. The shape of the

concentration profile can be seen with contours, shown in Figures 11 and 13, and the trend ahead of concentration can be seen in the plots. At $x/H = 15$ the amount of concentration was 0.5, 7, and 18.5 (mol/m^3) during 0.1, 0.3, and 0.6 (s), respectively. Comparing Figures 12 and 14, it is evident that the concentration in a high porosity collector would completely diffuse over time in comparison to a low porosity collector. The difference in the amount of concentration was 84 percent at the end of the solar collector for $t = 0.6$ (s). At $t = 0.6$ (s), all the collectors would be full in a low porous collector; however, this cannot be seen clearly for a high porous collector.

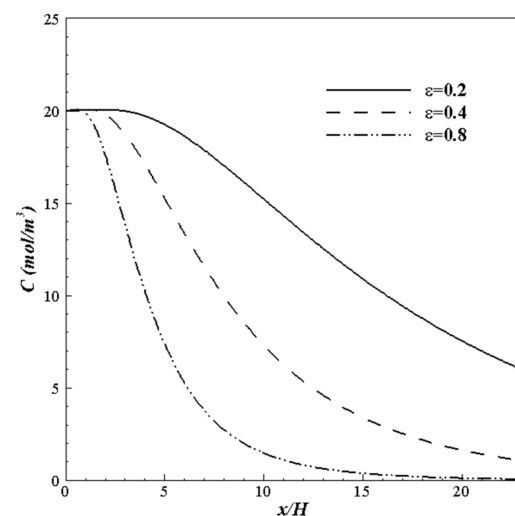**Figure 14.** The variation in concentration versus the length to height ratio of the porous collector for the three different times, with a high porosity coefficient of 0.8.

The variations in concentration versus the length to the height of the solar collector for the three different porosity coefficients of 0.2, 0.4, and 0.8 are shown at $t = 0.1$ s in Figure 15. As shown in this figure, the concentration diffusion was increased with a decreasing porosity. This was aligned with the accelerating flow in a smaller void space at a lower porosity coefficient. This phenomenon was also confirmed by the increasing pressure differences at low porosities presented in Figure 10.

Figure 15. The variation in concentration versus the length to height ratio of the porous collector for the three different porosity coefficients of 0.2, 0.4, and 0.8 at $t = 0.1$ *s*.

5. Conclusions

In the current study, the effects of porous media with different values of porosity and permeability on fluid flow, heat, and concentration parameters were calculated by a newly developed Brinkman equation into a solar collector. The main results of this work can be summarized as follows:

– The comparison between the non-temporal temperature variations with the experimental results in [5] shows good agreement, with maximum errors of 3%.
– The results of the present model are closer to the experimental data in [5] rather than to the numerical results in [5].
– Under constant permeability, the velocity decreases by decreasing the porosity. This is due to the presence of porosity in the collector, where the flow accelerates in the porous collector.
– By increasing the porosity coefficient, the velocity into the boundary layer decreases, and as a result, the thickness of the boundary layer is also decreased.
– In high porosity, according to the definition of porosity, which is the ratio of empty volume to total volume, the empty holes for fluid flow increase, the fluid acceleration is lower, and, therefore, the maximum speed of the ratio of the lower porosity coefficient will be lower.
– The porosity and permeability effects on the pressure drop along the collector are in accordance with a linear relationship that decreases with the increasing porosity and permeability of the pressure drop.
– According to the results, the drop in the pressure inside the porous collector increases closer to the porous collector, which results in higher thermal energy for faster pumping of the high-energy fluid and improves the heat transfer of the solar heat into the collector.
– With increasing pressure due to the porosity in the porous collector, it is possible to increase the temperature of the fluid without changing the phase in the porous collector.
– In the concentration distribution, coupled with developed Brinkman momentum equation, the gradient concentration is determined by the shear stress term near the wall.

Author Contributions: Conceptualization: S.A.F., M.R. and M.G.; methodology: S.A.F. and M.R.; software: S.A.F. and M.R.; validation: S.A.F. and M.R.; formal analysis: S.A.F., M.R. and M.G.; investigation: S.A.F., M.R. and M.G.; resources: M.G.; data curation: M.G.; writing—original draft preparation: S.A.F. and M.R.; writing—review and editing: S.A.F., M.R. and M.G. All authors have read and agreed to the published version of the manuscript.

Institutional Review Board Statement: Not applicable.

Informed Consent Statement: Not applicable.

Data Availability Statement: The data presented in this study are available on request from the corresponding author.

Conflicts of Interest: The authors declare no conflict of interest.

Nomenclature

P	$(\mathrm{kgm}^{-1}\mathrm{s}^{-2})$	Pressure
v	(ms^{-1})	Velocity
u	(ms^{-1})	Darcy's velocity

T	(K)	Temperature
C_P	$\left(\text{J}\cdot\text{kg}^{-1}\text{K}^{-1}\right)$	Heat capacity in constant pressure
H	(mm)	Height of the collector
h	$\left(\text{w}\cdot\text{m}^{-2}\text{K}^{-1}\right)$	Convection heat transfer coefficient
Nu		Nusselt number
q''	$(\text{W}\cdot\text{m}^{-2})$	Heat flux
K	(m^2)	Permeability
k	$\left(\text{w}\cdot\text{m}^{-1}\text{K}^{-1}\right)$	Conduction heat transfer coefficient
L	(mm)	Length of the collector
X	(mm)	Length
C	(mol/m^3)	Concentration
τ_F		Effective mass diffusivity coefficient
D_F	(m^2/s)	Fluid diffusivity coefficient
D_D	(m^2/s)	Dispersion coefficient
D_e	(m^2/s)	Total diffusivity coefficient
		Greek symbols
ρ	(kgm^{-3})	Density
μ	$(\text{kgm}^{-1}\text{s}^{-1})$	Dynamic viscosity
ε		Porosity coefficient
∇		Gradient
w		
in		
eff		
p		

References

1. Bars, M.L.; Worster, M.G. Interfacial conditions between a pure fluid and a porous medium: Implications for binary alloy solidification. *J. Fluid Mech.* **2006**, *550*, 149–173. [CrossRef]
2. Bayomy, A.M.; Saghir, M.Z. Experimental study of using c-Al2O3–water nanofluid flow through aluminum foam heat sink: Comparison with numerical approach. *Int. J. Heat Mass Transf.* **2017**, *107*, 181–203. [CrossRef]
3. Boomsma, K.; Poulikakos, D. On the elective thermal conductivity of a threedimensionally structured ¯uid-saturated metal foam. *Int. J. Heat Mass Transf.* **2001**, *44*, 827–836. [CrossRef]
4. Nield, D.A.; Bejan, A. *Convection in Porous Media*; Springer: New York, NY, USA, 2006.
5. Dukhan, N.; Chen, K.-C. Heat transfer measurements in metal foam subjected to constant heat flux. *Exp. Therm. Fluid Sci.* **2007**, *32*, 624–631. [CrossRef]
6. Dukhan, N.; Ratowski, J. Convection Heat Transfer Analysis for Darcy Flow in Porous Media: A New Two-Dimensional Solution. In Proceedings of the International Heat Transfer Conference, Washington, DC, USA, 8–13 August 2010; pp. 865–871. [CrossRef]
7. Furman, E.L.; Finkelstein, A.B.; Cherny, M.L. Permeability of Aluminium Foams Produced by Replication Casting. *Metals* **2013**, *3*, 49–57. [CrossRef]
8. Guo, L.; Yu, J. Dynamic bending response of double cylindrical tubes filled with aluminum foam. *Int. J. Impact Eng.* **2011**, *38*, 85–94. [CrossRef]
9. Hamdan, M. Single-phase flow through porous channels a review of flow models and channel entry conditions. *Appl. Math. Comput.* **1994**, *62*, 203–222. [CrossRef]
10. Lu, W.; Zhao, C.Y.; Tassou, S.A. Thermal analysis on metal-foam filled heat exchangers. Part I: Metal-foam filled pipes. *Int. J. Heat Mass Transf.* **2006**, *49*, 2751–2761. [CrossRef]
11. Mancin, S.; Zilio, C.; Diani, A.; Rossetto, L. Experimental air heat transfer and pressure drop through copper foams. *Exp. Therm. Fluid Sci.* **2012**, *36*, 224–232. [CrossRef]
12. Rezapour, M.; Fanaee, S.A. Thermal and fluid effects modeling of porous medium on hydrogen mixture with COMSOL. In Proceedings of the Hydrogen and Fuel Cell Conference, Tehran, Iran, 9 May 2017.
13. Nakayama, A.; Shenoy, A.V. Combined forced and free convection heat transfer in power-law fluidsaturated porous media. *Appl. Sci. Res.* **1993**, *50*, 83–95. [CrossRef]
14. Özgümüş, T.; Mobedi, M.; Özkol, Ü.; Nakayama, A. Thermal Dispersion in Porous Media—A Review on Approaches in Experimental Studies. In Proceedings of the 6th International Advanced Technologies Symposium, Elazığ, Turkey, 16–18 May 2011.
15. Pankaj, M.; Malipatil, A.S. Experimental Investigation of Pressure Drop & Heat Transfer Coefficient for Aluminium Metal Foams. *IOSR J. Mech. Civ. Eng.* **2016**, *13*, 33–38. [CrossRef]

16. Fanaee, S.A.; Rezapour, M. Analysis of the Fluid-Thermal Regime with the Developed Brinkman Model in a Porous Coil for Solar Energy Application. *Modares Mech. Eng.* **2019**, *19*, 855–863.

17. Zhong, W.; Xu, K.; Li, X.; Liao, Y.; Tao, G.; Kagawa, T. Determination of pressure drop for air flow through sintered metal porous media using a modified Ergun equation. *Adv. Powder Technol.* **2016**, *27*, 1134–1140. [CrossRef]

18. Yang, C.; Nakayama, A. A synthesis of tortuosity and dispersion in effective thermal conductivity of porous media. *Int. J. Heat Mass Transf.* **2010**, *53*, 3222–3230. [CrossRef]

19. Diersch, H.J.G. *Finite Element Modeling of Flow, Mass and Heat Transport in Porous and Fractured Media*; Springer: Berlin/Heidelberg, Germany, 2014.

20. Xu, H.; Zhao, C.; Vafai, K. Analytical study of flow and heat transfer in an annular porous medium subject to asymmetrical heat fluxes. *Heat Mass Transf.* **2017**, *53*, 2663–2676. [CrossRef]

21. Dushin, V.R.; Nikitin, V.F.; Legros, J.C.; Silnikov, M.V. Mathematical modeling of flows in porous media. *WSEAS Trans. Fluid Mech.* **2014**, *9*, 116–130.

22. Nakayama, A.; Shenoy, A.V. Non-Darcy Forced Convective Heat Transfer in a Channel Embedded In a Non-Newtonian Inelastic Fluid-Saturated Porous Medium. *Can. J. Chem. Eng.* **1993**, *71*, 168–173. [CrossRef]

23. Cummins, B.M.; Chinthapatla, R.; Ligler, F.S.; Walker, G.M. Time-Dependent Model for Fluid Flow in Porous Materials with Multiple Pore Sizes. *Anal. Chem.* **2017**, *89*, 4377–4381. [CrossRef]

24. Fanaee, S.A.; Rezapour, M. The Modeling of Constant/Variable Solar Heat Flux Into a Porous Coil With Concentrator. *J. Sol. Energy Eng.* **2019**, *142*, 1–12. [CrossRef]

25. Zehforoosh, A.; Hossainpour, S.; Tahery, A.A. Numerical Investigation of Forced Convection Heat Transfer for Laminar Flow in Various Parallel Porous Channels. *Int. J. Innov. Manag. Technol.* **2010**, *1*, 252.

26. Dukhan, N.; Bağcı, Ö.; Özdemir, M. Thermal development in open-cell metal foam: An experiment with constant wall heat flux. *Int. J. Heat Mass Transf.* **2015**, *85*, 852–859. [CrossRef]

27. Zafariyan, S.; Fanaee, A.; Mohammadzadeh, A. The Investigation of Thermal and Solutal Secondary Effects on MHD Convective Transfer Past a Vertical Surface in a Porous Medium. *Arab. J. Sci. Eng.* **2013**, *38*, 3211–3220. [CrossRef]

28. Zafariyan, S.; Fanaee, S.A. MHD Mixed Convective Flow Past a Vertical Plate Embedded in a Porous Medium with Radiation Effects and Convective Boundary Condition Considering Chemical Reaction. *Cankaya Univ. J. Sci. Eng.* **2013**, *10*, 123–136.

29. Ferchichi, S.; Kessentini, H.; Morales-Ruiz, S.; Rigola, J.; Bouden, C.; Oliva, A. Thermal and fluid dynamic analysis of Direct Steam Generation Parabolic Trough Collectors. *Energy Convers. Manag.* **2019**, *196*, 467–483. [CrossRef]

30. Rezapour, M.; Gholizadeh, M. Analysis of methanol thermochemical reactor with volumetric solar heat flux based on Parabolic Trough Concentrator. *Renew Energy* **2021**, *180*, 1088–1100. [CrossRef]

31. Yang, S.; Ordonez, J. 3D thermal-hydraulic analysis of a symmetric wavy parabolic trough absorber pipe. *Energy* **2019**, *189*, 116320. [CrossRef]

32. Deymi-Dashtebayaz, M.; Rezapour, M. The effect of using nanofluid flow into a porous channel in the CPVT under transient solar heat flux based on energy and exergy analysis. *J. Therm. Anal. Calorim.* **2020**, *145*, 507–521. [CrossRef]

33. Deymi-Dashtebayaz, M.; Rezapour, M.; Farahnak, M. Modeling of a novel nanofluid-based concentrated photovoltaic thermal system coupled with a heat pump cycle (CPVT-HP). *Appl. Therm. Eng.* **2021**, *201*, 117765. [CrossRef]

34. Bårdsgård, R.; Kuzmenkov, D.M.; Kosinski, P.; Balakin, B.V. Eulerian CFD model of direct absorption solar collector with nanofluid. *J. Renew Sustain. Energy* **2020**, *12*, 033701. [CrossRef]

35. Huang, G.; Wang, K.; Curt, S.R.; Franchetti, B.; Pesmazoglou, I.; Markides, C.N. On the performance of concentrating fluid-based spectral-splitting hybrid PV-thermal (PV-T) solar collectors. *Renew Energy* **2021**, *174*, 590–605. [CrossRef]

36. Alves, P.; Fernandes, J.F.; Torres, J.P.N.; Branco, P.C.; Fernandes, C.; Gomes, J. From Sweden to Portugal: The effect of very distinct climate zones on energy efficiency of a concentrating photovoltaic/thermal system (CPV/T). *Sol. Energy* **2019**, *188*, 96–110. [CrossRef]

37. Ravanbakhsh, M.; Deymi-Dashtebayaz, M.; Rezapour, M. Numerical investigation on the performance of the double tube heat exchangers with different tube geometries and Turbulators. *J. Therm. Anal. Calorim.* **2022**, *147*, 11313–11330. [CrossRef]